# A novel multifunctional carrier with magnetic-NIR luminescent-microwave heating characteristics for drug delivery

Ziyang Jiang [a], Hongxia Peng [a,*], Wenhui Chen [a], Fabiao Yu [b,**]

[a] *Hunan Provincial Key Laboratory of Fine Ceramics and Powder Materials, Hunan University of Humanities, Science and Technology, Lou'di, Hunan, 417000, PR China*
[b] *Key Laboratory of Hainan Trauma and Disaster Rescue, The First Affiliated Hospital of Hainan Medical University, Hainan Medical University, Haikou, 571199, China*

## ARTICLE INFO

## ABSTRACT

We constructed a novel core–shell structured $Fe_3O_4@WO_{3-x(x=0\sim1)}@GdF_3$: Yb/Er nanoparticles with magnetic-NIR luminescent-microwave heating characteristics used as drug carrier to investigate the loading and controllable release properties of the chemotherapeutic drug doxorubicin (DOX). The porous surface of $Fe_3O_4@WO_{3-x(x=0\sim1)}@GdF_3$:Yb/Er nanoparticles can store DOX molecules by means of physical adsorption. The $Fe_3O_4$ core and $GdF_3$: Yb/Er shell functioned successfully for magnetic targeting (1.40 emu•$g^{-1}$) and NIR fluorescence imaging (NIR 650–850 nm), respectively. The introduction of $WO_{3-x(x=0\sim1)}$ with LSPR effect enhanced the luminescence of near-infrared region of $Fe_3O_4@WO_{3-x(x=0\sim1)}@GdF_3$:Yb/Er nanoparticles successfully. In addition, the $WO_{3-x(x=0\sim1)}$ acts as a good microwave absorber with excellent microwave thermal response property for microwave triggered drug release (the DOX release of 12% under microwave irradiation for 10 s outclass the 2% within 1 h without microwave irradiation release). The release profile could be controlled by the duration and number of cycles of microwave application. Moreover, it can monitor the drug release process in real time under the guidance of near infrared imaging, which is convenient to evaluate the therapeutic effect. This work provides a new idea for realizing the visual real-time dynamic monitoring of the chemotherapy process and realizing "positioning-timing-quantitative" administration, thus improving the chemotherapy effect.

## 1. Introduction

How to effectively treat cancers, which are of high complexity and diversity, remains a severe challenge. As one of common methods clinically used to treat cancers, chemotherapy is a therapeutic method that kills tumor cells and represses their growth and reproduction using chemical drugs. Chemotherapy, a systemic therapeutic method, can exert therapeutic actions on primary foci, metastasis foci, and subclinical metastasis foci [1,2]. However, chemical drugs fail to distinguish normal tissue cells from tumor and cancerization cells or monitor the drug delivery in a real-time fashion. Consequently, such chemical drugs will kill normal cells and immune cells while killing tumor cells, thus triggering various toxic and side effects, degrading the general survival quality of patients, and even resulting in the involuntary discontinuance of the treatment due to their intolerance [3,4]. Hence, a brand-new targeted controlled mode of drug delivery has been proposed internationally, namely, the site or organ of lesion is treated in a targeted and positioned way to selectively kill cancer cells while not harming normal cells, thereby reaching the efficient treatment goal [5,6]. Given this, the research and development of new-type multifunctional drug carriers is still the difficulty in realizing "specific and time and quantity-controlled" drug delivery and further improving the chemotherapeutic efficacy.

In recent years, it has been found by researchers that magnetic nanoparticle-luminescent nanoparticle composite new "two-in-one" difunctional nanoparticles, which simultaneously have two characteristics in one entity, cannot only manipulate, as drug carriers, target tumor sites using external magnetic fields but also provides high-resolution images via the fluorescence imaging techniques and timely monitor the drug release process [7,8]. Such new-type nanoparticles play a significant role in precision chemotherapy. The current research focus has been on magnetic@up-conversion luminescent difunctional materials designed and synthesized using the advantages like the large magnetic moment, high relaxation efficiency, low toxicity and low cost
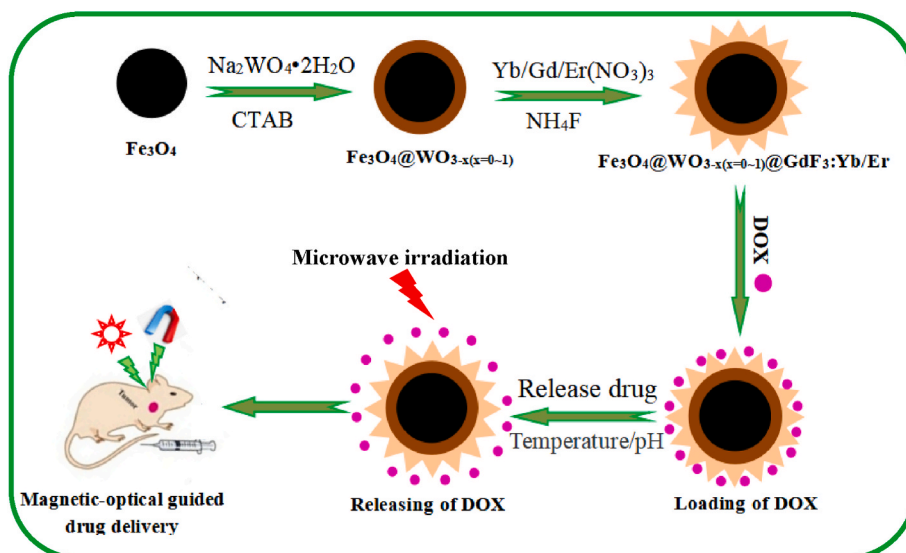
**Fig. 1.** Schematic diagram of the synthesis process of $Fe_3O_4@WO_{3-x(x\ =\ 0\sim1)}@GdF_3$:Yb/Er nanoparticles.

of magnetic $Fe_3O_4$ as well as the characteristics like good photochemical stability, high quantum yield, deep tissue part imaging and low bio-toxicity of rare earth up-conversion luminescent (UCL) materials [9, 10]. For instance, $Fe_3O_4@NaYF_4$ (Yb, Er) and $Fe_3O_4@NaYF_4$ (Yb, Tm) difunctional materials can serve a drug carriers guided by magnetic-fluorescence imaging [11]. Despite the certain research progress regarding "$Fe_3O_4$@UCL magnetic-upconversion luminescent difunctional nanocomposite", nevertheless "quantity and time-controlled" drug release cannot be effectively realized due to the lack of their controllability. Moreover, the tissue penetration depth is insufficient because of short emitted light wavelength (visible light region). With the increasing depth of biological tissues, moreover, the light signal will be weakened, thus leading to scientific problems like the low signal to noise ratio (SNR) in deep tissues.

Given the above problems, an intermediate layer with both microwave heating characteristics and local surface plasmon resonance effect was introduced into the $Fe_3O_4$@UCL magnetic-upconversion luminescent difunctional nanocomposite to construct a new-type inorganic nanocarrier featured by magnetic targeting, NIR fluorescence imaging and microwave stimulation-based "specific and time and quantity-controlled" drug release. This new-type nanocarrier could improve the therapeutic effect of chemotherapeutics and relieve the toxic and side effects of chemotherapeutics on human tissues in human body.

Microwave absorbing materials have been applied in the field of biological medicine more and more extensively by virtue of rapid local heating, good penetrability into biological tissues, high safety, and easy control. Microwave absorbing materials mainly include nanometal and alloy wave-absorbing materials [12], carbon nanotube wave-absorbing materials [13], nano-ceramic wave-absorbing materials [14], nanometer oxide wave-absorbing materials [15], nano-silicon carbide absorbents [16], etc. Therein, simply structured and high-performance nanometer oxide microwave-absorbing materials, such as $Fe_3O_4$ [17], $WO_{3-x(x\ =\ 0\sim1)}$ [18], $MoO_{3-x(x\ =\ 0\sim1)}$ [19], ZnO [20], $TiO_2$ [21], $SnO_2$ [22] have been extensively investigated. According to research findings, $WO_{3-x(x\ =\ 0\sim1)}$ nanoparticles can absorb microwaves of a certain frequency and convert them into heat energy due to the superior microwave absorptivity and microwave thermal response characteristics [23]. Compared with visible lights, moreover, NIR lights are absorbed and scattered weakly by biological tissues without any evident auto-fluorescence, so NIR lights can be used as detection signals to reduce background interference and signal attenuation [24,25]. Studies have shown that $WO_{3-x(x\ =\ 0\sim1)}$ nanoparticles can enhance the excitation and emission intensity of rare earth fluoride NIR luminescent materials

using their good local surface plasmon resonance effect [26–28].

Based on the above studies, a new type of core-shell $Fe_3O_4@WO_{3-x(x\ =\ 0\sim1)}@$ $GdF_3$:Yb/Er magnetic-microwave absorbing-NIR luminescent multifunctional nanoparticles were established, and their structures, morphologies and performance were explored. The $WO_{3-x(x\ =\ 0\sim1)}$ intermediate layer impeded the direct contact between magnetic materials and NIR luminescent materials. The NIR luminescent intensity of the $GdF_3$:Yb/Er layer could be strengthened by the LSPR effect of $WO_{3-x(x\ =\ 0\sim1)}$ nanoparticles, but moreover, drugs could be released in controlled time and quantity by virtue of the microwave absorptivity and microwave thermal conversion characteristics of $WO_{3-x(x\ =\ 0\sim1)}$ so as to acquire a new-type inorganic nanocarrier characterized by magnetic targeting, NIR fluorescence imaging and microwave heating-based "specific and time and quantity-controlled" drug release. The synthesis of this nanocarrier and the controllable drug delivery process are displayed in Fig. 1.

## 2. Experimental section

### 2.1. Reagents and instruments

Rare earth oxides ($Gd_2O_3$, $Yb_2O_3$, $Er_2O_3$ 99.99%) were purchased from Science and Technology Parent Company of Changchun Institute of Applied Chemistry. Ferric chloride hexahydrate (purity 99.0%, $FeCl_3 \cdot 6H_2O$), sodium acetate (purity 99.0%, $CH_3COONa$), ethylene glycol (purity 96.0%, EG), and poly (ethylene glycol) (PEG Mw = 20000) were purchased from Beijing Chemical Reagent Limited China. Sodium tungstate dihydrate ($Na_2WO_3 \cdot 2H_2O$, purity 99%) was purchased from Tianjin Kemiou Chemical Reagent Co. Ltd (Tianjin, China). Hexadecyltrimethyl ammonium bromide ($C_{19}H_{42}BrN$, CTAB, purity 99%), sodium hydroxide (NaOH, purity 99%), concentrated hydrochloric acid (HCl, 38%), and ammonium hydroxide ($NH_3 \cdot H_2O$, AR) were purchased from Kaixin Chemical Reagent Co. Ltd (Hunan, China). Ammonium fluoride ($NH_4F$) was purchased from Beijing Chemical Works. All the above chemical reagents were of analytical grade and used without further purification. Rare earth salts ($Gd(NO_3)_3$, $Yb(NO_3)_3$, $Er(NO_3)_3$) were prepared by dissolving the corresponding rare earth oxides ($Gd_2O_3$, $Yb_2O_3$, $Er_2O_3$, 99.99%) in nitric acid and evaporating their solutions.

X-ray diffraction (XRD) patterns of the samples were analyzed under AXS D8 Advance Diffractometer (Bruker, Bremen, Germany) with Cu–K α radiation (λ = 0.15406 nm) at 40 kV and 40 mA; the morphology and size of the samples were observed via JEM-2100 scanning electron
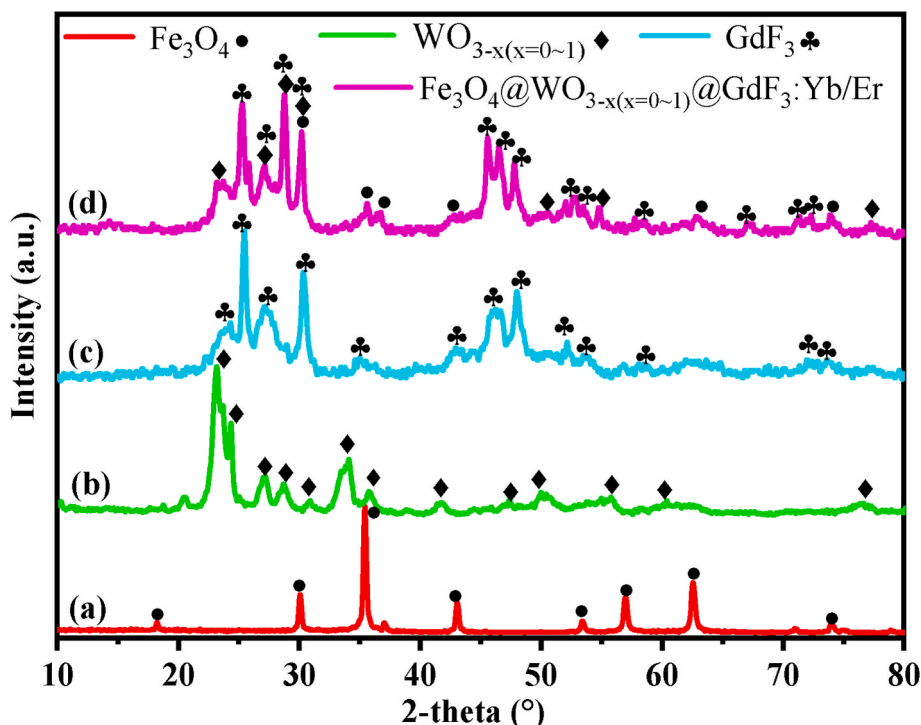
**Fig. 2.** XRD patterns of the samples: (A) $Fe_3O_4$, (B) $WO_{3-x (x = 0~1)}$, (C) $GdF_3$: Yb/Er and (D) $Fe_3O_4@WO_{3-x (x = 0~1)}@GdF_3$: Yb/Er nanoparticles.

microscope SEM (Supra 55, Carl Zeiss, Germany) with energy dispersive X-ray spectrum (EDS); Transmission electron microscopy (TEM), EDS, HRTEM and SAED (FEI, Tecnai T20, Netherland) were carried out after dissolving all samples in ethanol and mounted them in a copper grid. The UV/Vis/Infrared light absorption performance was analyzed by UV 3600 spectrometer with a scanning range of 1200–200 nm (Hitachi, Japan). The luminescence properties of the samples were tested by the F-4500 fluorescent spectrometer made by Hitachi Company in Japan. The measurement range was 500–900 nm, the scanning rate was 1200 nm $min^{-1}$, the step size was 0.2 nm 980 nm were used as the excitation sources. Magnetization measurements were performed on an MPMSSQUID XL superconducting quantum interference device (SQUID) magnetometer at 300 K (Quantum Design, America). Microwave to heat responsive properties and drug release with microwaves were measured using a MCR-3 microwave reactor.

### 2.2. Experiment method

#### 2.2.1. Preparation of $Fe_3O_4@WO_{3-x (x = 0~1)}$ nanoparticles

Magnetic $Fe_3O_4$ nanoparticles were prepared by the solvothermal method [29]. $WO_{3-x (x = 0~1)}$ was layered on the surface of the magnetic $Fe_3O_4$ nanoparticles using a direct precipitation method. In a typical procedure, 0.1 g of the as-prepared $Fe_3O_4$ nanoparticles was dispersed in 75 mL of CTAB (0.364 g) solution. The mixture was sonicated for 15 min, followed by the addition of 50 mL of $Na_2WO_3 \cdot 2H_2O$ (3.3 g) solution. Then, hydrochloric acid and ammonia solution were added with constant stirring to adjust the pH value to 2, followed by stirring for 1 h at room temperature. The resulting products were separated with a magnet, thoroughly washed several times with ethanol and deionized water, and dried at 60 °C overnight. The dried particles were then calcinated for 2 h at 500 °C. The resulting products were the $Fe_3O_4@WO_{3-x (x = 0~1)}$ core–shell structured nanoparticles.

#### 2.2.2. Preparation of $Fe_3O_4@WO_{3-x (x = 0~1)}@GdF_3$: Yb/Er nanoparticles

$GdF_3$: Yb/Er luminescent shell was coated on $Fe_3O_4@WO_{3-x (x = 0~1)}$ nanoparticles by a direct precipitation method. In a typical procedure, 0.1 g of the as-prepared $Fe_3O_4@WO_{3-x (x = 0~1)}$ nanoparticles were

dispersed in 100 mL of water. Then, 3.2 mL of $Gd(NO_3)_3$, 1.2 mL of Er $(NO_3)_3$ and 3.6 mL of Yb $(NO_3)_3$ solutions were added. The mixture was sonicated for 20 min, followed by the addition of 10 mL of 0.6 mol $L^{-1}$ $NH_4F$ solution and then, this mixture was heated to 75 °C under vigorous mechanical stirring. After 2 h, the resultant products were separated with a magnet, thoroughly washed with ethanol and deionized water several times, and further dried at 60 °C overnight. Finally, $Fe_3O_4@WO_{3-x (x = 0~1)}@GdF_3$: Yb/Er nanocomposites were obtained.

#### 2.2.3. Drug loading

The doxorubicin hydrochloride (DOX) was dissolved in deionized water and prepared into DOX aqueous solution with a mass concentration of 2 g/L. Then, $Fe_3O_4@WO_{3-x (x = 0~1)}@GdF_3$:Yb/Er nanoparticles was dispersed in physiological saline to prepare the suspension solutions with a mass concentration of 10 g/L 1 mL of DOX aqueous solution was slowly added to the above suspension solutions, and magnetic stirring was carried out. The clear solutions were taken at 0, 30, 60, 90, 150 and 210 min respectively and the concentration of DOX in the solution was measured by ultraviolet spectrophotometer (quartz colorimetric dish). The drug loading of nanoparticles was calculated by Lambert-Beer law.

$$R_M = M_{ads}/M_{add} \times 100\%$$

Among them, $R_M$ is the loading rate of the drug doxorubicin. $M_{ads}$ is the mass of DOX loaded onto the surface of the carrier, and $M_{add}$ is the initial amount of DOX in the process of drug loading.

#### 2.2.4. Drug release

To determine the critical temperature for release of the VP-16, we heated 2 mL $Fe_3O_4@WO_{3-x (x = 0~1)}@GdF_3$:Yb/Er-DOX (at 0.2 mg/mL) in the sodium chloride solution in a water bath at three temperatures (room temperature, 37 and 42 °C). The sample was heated for 90 min and the UV–vis intensity was measured. Release behavior of DOX was investigated at pH 5.0 (approximate pH in endosomes or lysosomes), pH 6.0 (pH of the environment around the tumor) and pH 7.0 (pH of physiological blood). $Fe_3O_4@WO_{3-x (x = 0~1)}@GdF_3$:Yb/Er-DOX nanoparticles (20 mg) were dispersed in physiological saline (pH 7, 20 mL)
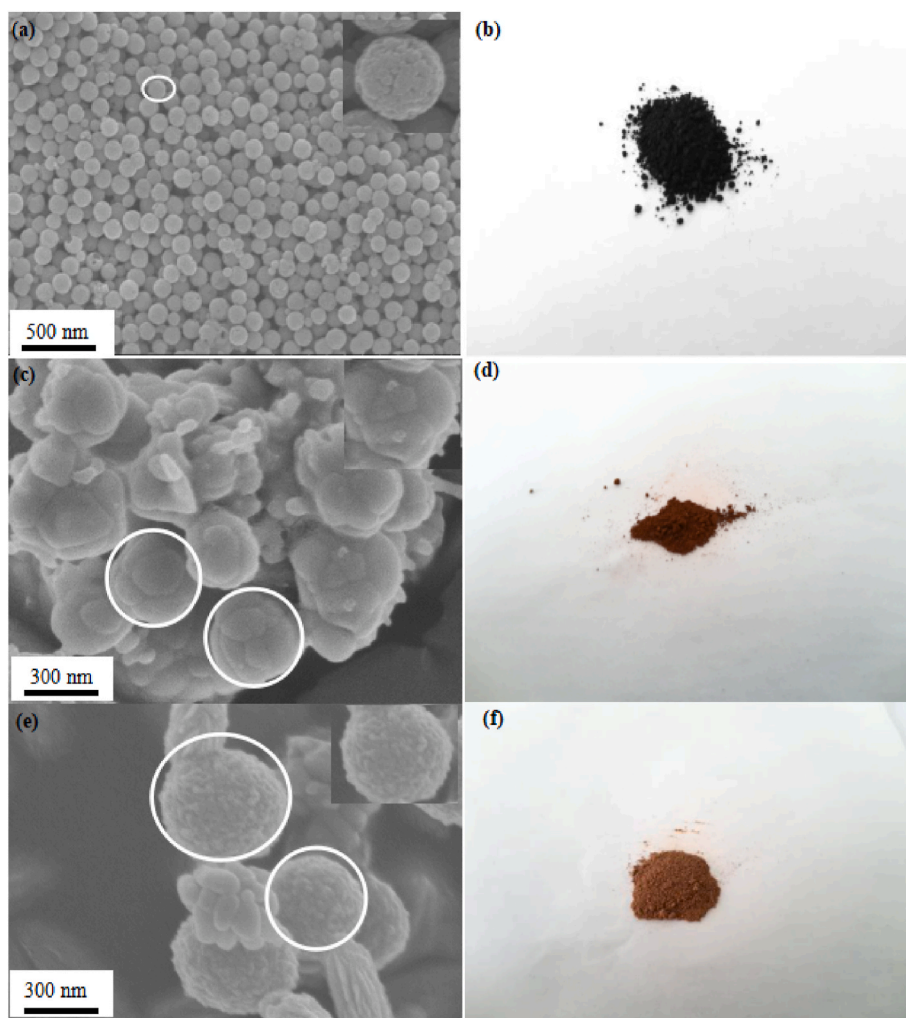
**Fig. 3.** SEM images of (a) Fe$_3$O$_4$ (c) Fe$_3$O$_4$@WO$_{3-x\ (x\ =\ 0\sim1)}$ and (e) Fe$_3$O$_4$@WO$_{3-x\ (x\ =\ 0\sim1)}$@GdF$_3$: Yb/Er; (b) (d) (f) Powder pictures of the three sample, respectively.

and transferred into a dialysis syringe. The dialysis syringe was then immersed in 95 mL physiological saline at pH 5.0, 6.0 and 7.0. The release medium was continuously agitated with a stirrer at 37 °C. At predetermined time intervals, 2 mL of the external medium was collected and replaced with the same fresh physiological saline. The withdrawn solution was properly diluted and monitored for DOX content at 503 nm using UV–vis spectrophotometer.

The amount of DOX released after five on/off cycles of the microwave emitter was evaluated to study the nature of the triggered release. We irradiated 2 mL samples of Fe$_3$O$_4$@WO$_{3-x(x = 0\sim1)}$@GdF$_3$:Yb/Er-DOX (at 0.2 mg/mL) in the sodium chloride solution with microwaves for five on/off cycles of the microwave emitter. During each cycle, the sample was first irradiated for 10, 20, 40, 60, 80 s and then the microwave was turned off. The sample was then kept at room temperature for 1 h and the UV–vis intensity of the sample was measured.

## 3. Results and discussion

### 3.1. XRD analysis

The XRD spectra of the sample is exhibited in Fig. 2. A total of five diffraction peaks appeared on the curve (a) at 2θ values of 30.08°, 35.3°, 43.2°, 57.2° and 62.4°. Compared with the Fe$_3$O$_4$ standard card (PDF#19–0629), the position and relative intensity of such diffraction peaks were identical with the standard card, indicating that the sample was Fe$_3$O$_4$. The curve (b) was the diffraction curve of WO$_{3-x(x\ =\ 0\sim1)}$

nanocrystals, which was consistent with the WO$_{3-x(x\ =\ 0\sim1)}$ standard card (PDF#41–0905) in both position and relative intensity. The curve (c) was the diffraction curve of GdF$_3$:Yb/Er nanocrystals. In addition to the diffraction peaks of Fe$_3$O$_4$ and WO$_{3-x(x\ =\ 0\sim1)}$, new diffraction peaks appeared at 2θ values of 23.9°, 26.1°, 27.7°, 31.5°, 35.8°, 44.0°, 49.4° and 55.3° in the curve (d). In comparison with the standard card (PDF#49–1804) of GdF$_3$:Yb/Er, the position and relative intensity of these new diffraction peaks were found to be identical with those of the standard card, indicating that WO$_{3-x(x\ =\ 0\sim1)}$ and GdF$_3$:Yb/Er were successfully cladded on the surface of Fe$_3$O$_4$. By comparing the curves (a), (b), (c) and (d), it could be discovered that the relative intensity of diffraction peaks of Fe$_3$O$_4$ and WO$_{3-x(x\ =\ 0\sim1)}$ in the curve (d) were evidently weakened and even some peaks disappeared. The main reason was that Fe$_3$O$_4$ was cladded by both WO$_{3-x(x\ =\ 0\sim1)}$ and GdF$_3$:Yb/Er, thus reducing the relative intensity of diffraction peaks of Fe$_3$O$_4$ and WO$_{3-x(x\ =\ 0\sim1)}$. The above results proved that the Fe$_3$O$_4$@WO$_{3-x(x\ =\ 0\sim1)}$@GdF$_3$:Yb/Er nanoparticles were successfully prepared.

### 3.2. SEM analysis

The SEM images of Fe$_3$O$_4$, Fe$_3$O$_4$@WO$_{3-x(x\ =\ 0\sim1)}$ and Fe$_3$O$_4$@WO$_{3-x(x\ =\ 0\sim1)}$@ GdF$_3$:Yb/Er nanoparticles are as shown in Fig. 3. It could be observed from Fig. 3(a) that Fe$_3$O$_4$ nanoparticles were spherical and uniformly distributed with a particle size of about 200 nm and a rough surface. In addition, it could be clearly seen from the illustration in Fig. 3 (a) (inset) that the surface structure was poorly compact. As observed
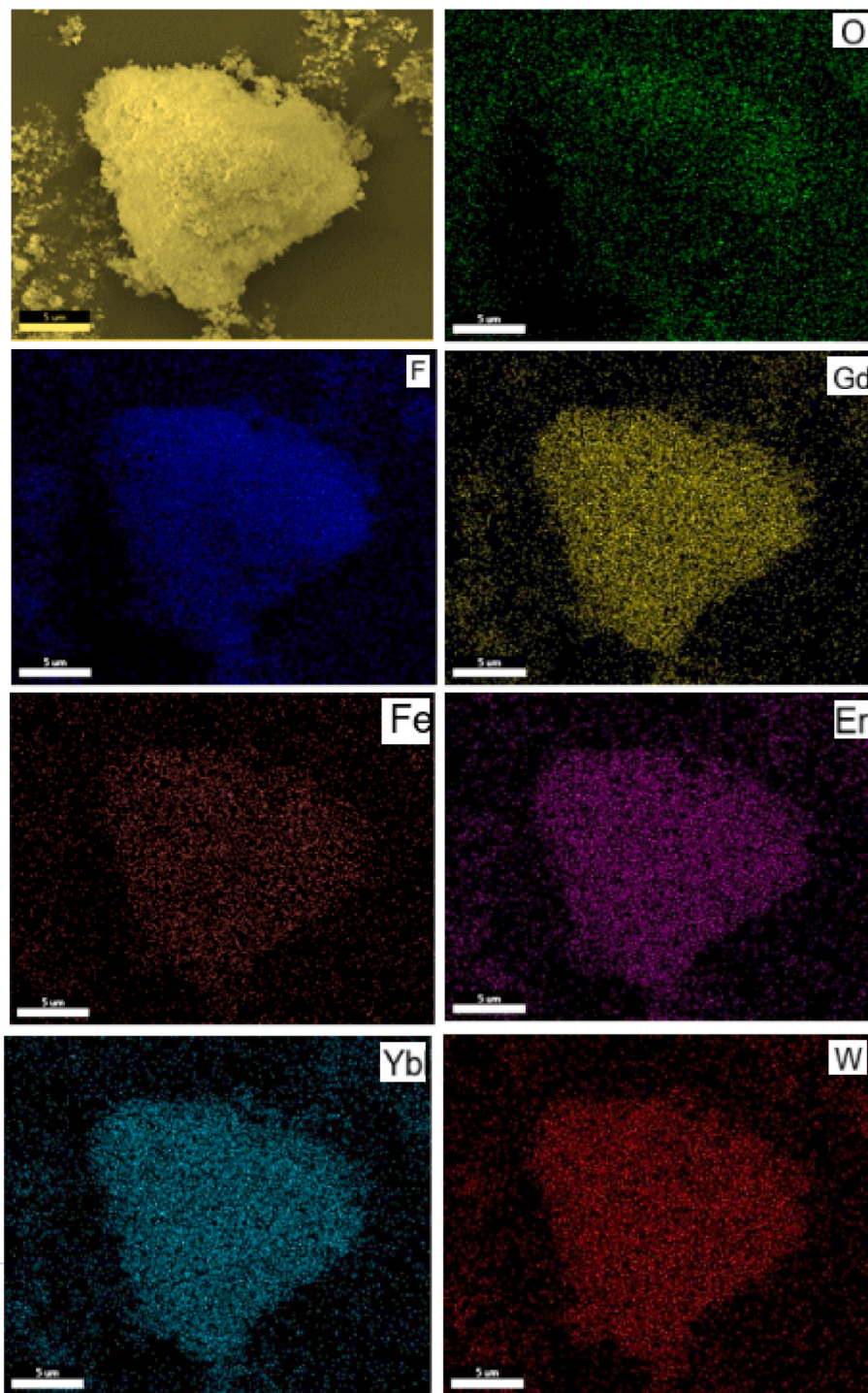
**Fig. 4.** Energy dispersive X-ray (EDX) mapping of $Fe_3O_4@WO_{3-x(x\ =\ 0\sim1)}@GdF_3$:Yb/Er nanoparticles.

from Fig. 3(c), the size of $Fe_3O_4$ nanoparticles was evidently enlarged and the surface became compact and smooth after one layer of $WO_{3-x(x\ =\ 0\sim1)}$ nanocrystals were cladded. It could be known from Fig. 3(e) that compared with $Fe_3O_4@WO_{3-x(x\ =\ 0\sim1)}$ nanoparticles, the surface of $Fe_3O_4@WO_{3-x(x\ =\ 0\sim1)}@GdF_3$:Yb/Er nanoparticles was rough with an enlarged particle size. In addition, it could be obviously seen from the illustration in Fig. 3(e) (inset) that many small $GdF_3$:Yb/Er nanocrystals were uniformly deposited on the surface of $Fe_3O_4@WO_{3-x(x\ =\ 0\sim1)}$ nanoparticles, also proving that $GdF_3$:Yb/Er nanocrystals were successfully deposited on the surface of $Fe_3O_4@WO_{3-x(x\ =\ 0\sim1)}$ nanoparticles. Moreover, it could be seen from Fig. 3(b)(d)(f) that with the

increase in cladding layers, the powder color gradually faded, manifesting that black $Fe_3O_4$ nanoparticles were successfully cladded layer by layer and $Fe_3O_4@WO_{3-x(x\ =\ 0\sim1)}@GdF_3$:Yb/Er core-shell nanoparticles were finally prepared.

The EDX element analysis was performed (Fig. 4) to further determine the components of $Fe_3O_4@WO_{3-x(x\ =\ 0\sim1)}@GdF_3$:Yb/Er nanoparticles. The distribution diagram of O, Fe, W, Gd, Yb, F and Er elements is displayed in Fig. 4. It could be seen that all elements were uniformly distributed, and EDX and SEM analyses further confirmed the formation of the nanocomposites.
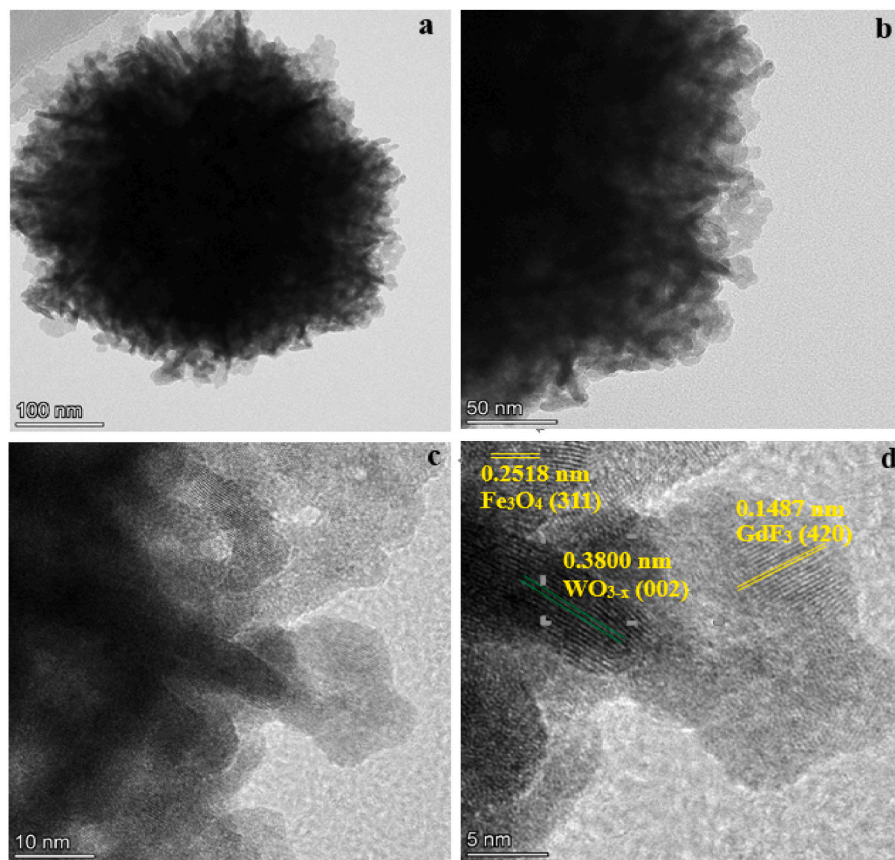
**Fig. 5.** (a,b) TEM, (c,d) HRTEM images of Fe$_3$O$_4$@WO$_{3-x(x = 0\sim1)}$@GdF$_3$:Yb/Er nanoparticles.

### 3.3. TEM analysis

The morphologies and core-shell structures of Fe$_3$O$_4$@WO$_{3-x(x = 0\sim1)}$@ GdF$_3$:Yb/Er nanoparticles were respectively subjected to TEM analysis in order to observe their morphologies and cladding state more clearly. The low-resolution TEM imaging of Fe$_3$O$_4$@WO$_{3-x(x = 0\sim1)}$@GdF$_3$:Yb/Er nanoparticles is displayed in Fig. 5(a and b). It could be seen that the Fe$_3$O$_4$@WO$_{3-x(x = 0\sim1)}$@GdF$_3$:Yb/Er nanoparticles were spherical with a particle size of about 200 nm, a rough and uneven surface, and poor compactness.

Fig. 5(c and d) presents the high-resolution TEM imaging of Fe$_3$O$_4$@WO$_{3-x(x = 0\sim1)}$@ GdF$_3$:Yb/Er nanoparticles. The core-shell structure was observed according to the core-shell difference in the aspect of contrast in the figure. The black area denoted Fe$_3$O$_4$ that could penetrate electron beams poorly, while WO$_{3-x(x = 0\sim1)}$ and GdF$_3$: Yb/Er of the shell layer showed good penetrability for electron beams, as manifested by the light gray area in the figure. It could be clearly observed from Fig. 5 (c,d) that small rodlike WO$_{3-x(x = 0\sim1)}$ nanocrystals and spherical GdF$_3$:Yb/Er nanocrystals were cladded on the Fe$_3$O$_4$ surface layer by layer. Moreover, lattice lines could be clearly observed in Fig. 5(d), the interplanar crystal spacing in the shell area was 0.148 nm, and that in the core area was 0.2518 and 0.3800 nm, respectively, which corresponded to the (420) face of GdF$_3$, the (311) face of Fe$_3$O$_4$, and the (002) face of WO$_{3-x(x = 0\sim1)}$ in the corresponding structure, respectively. No other obvious lattice lines were observed. The analysis results showed that the sample was of a well-crystallized core-shell structure.

The composition of the Fe$_3$O$_4$@WO$_{3-x(x = 0\sim1)}$@GdF$_3$:Yb/Er nanoparticles was determined through EDX analysis, as shown in Fig. 6. Fig. 6 is the distribution map of Fe, W, O, Gd, F, Er, and Yb. All the elements were evenly distributed. TEM and EDX analysis further confirmed the formation of the nanocomposites.

### 3.4. UV–Vis–NIR analysis

LSPR is a collective oscillation phenomenon of free electrons on the metal surface under the excitation of incident lights (electromagnetic waves), which is macroscopically manifested by the light absorption of metallic oxide particles. The UV–Vis–NIR light absorption spectrogram of Fe$_3$O$_4$, WO$_{3-x(x = 0\sim1)}$, Fe$_3$O$_4$@WO$_{3-x(x = 0\sim1)}$, GdF$_3$:Yb/Er and Fe$_3$O$_4$@WO$_{3-x(x = 0\sim1)}$@GdF$_3$:Yb/Er nanoparticles is exhibited in Fig. 7. It could be known that compared with Fe$_3$O$_4$, WO$_{3-x(x = 0\sim1)}$, Fe$_3$O$_4$@WO$_{3-x(x = 0\sim1)}$ and GdF$_3$:Yb/Er nanoparticles, Fe$_3$O$_4$@WO$_{3-x(x = 0\sim1)}$@GdF$_3$:Yb/Er nanoparticles showed a strong absorption peak within 200–1200 nm, indicating that Fe$_3$O$_4$@WO$_{3-x(x = 0\sim1)}$@GdF$_3$:Yb/Er nanoparticles displayed superior light absorptivity and favorable local surface plasmon resonance effect within the UV–Vis-IR region. The energy absorbed by WO$_{3-x(x = 0\sim1)}$ could be transferred to the GdF$_3$:Yb/Er shell via the LSPR effect, thus the electron transition from an excited state to a steady state and further enhance their luminescence properties. Meanwhile, the introduced WO$_{3-x(x = 0\sim1)}$ nanoparticles could also weaken the magnetic-optic quenching effect triggered by the direct contact between magnetic core and luminescent shell, thereby preventing the luminescence properties of GdF$_3$:Yb/Er from weakening. The LSPR of WO$_{3-x(x = 0\sim1)}$ nanoparticles was ascribed to the vibration of free carriers caused by O$^{2-}$ vacancies. The density of free carriers could be calculated through the Mie-Drude theory [29]:

$$N_h = \frac{\varepsilon_0 m_h (1 + 2\varepsilon_m)\left(\omega_{sp}^2 + \Upsilon^2\right)}{e^2} \tag{1}$$

Where $\varepsilon_0$ and $\varepsilon_m$ denote the dielectric constants of free space and environmental medium, respectively; $e$ and $m_h$ stand for the charge of elements and the effective mass of vacancies, respectively; $m_h$ approximately equals 0.8$m_0$ ($m_0$ is the electron mass); $W_{sp}$ is the energy
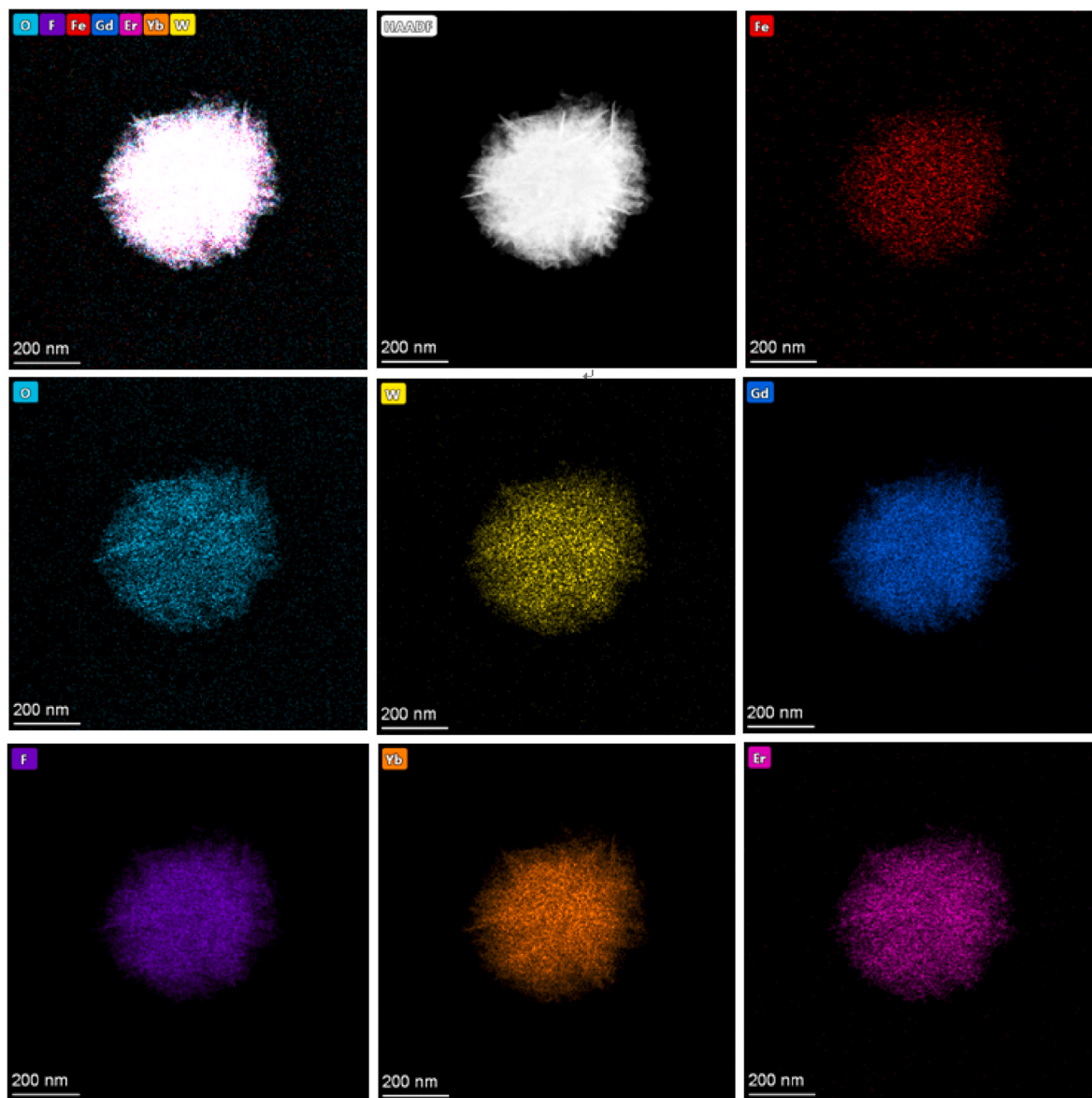
**Fig. 6.** (a) TEM images of $Fe_3O_4$@$WO_{3-x(x = 0\sim1)}$@$GdF_3$:Yb/Er nanoparticles; (b–h) energy dispersive X-ray (EDX) mapping of $Fe_3O_4$@$WO_{3-x(x = 0\sim1)}$@$GdF_3$:Yb/Er nanoparticles.

of LSPR; $\gamma$ represents the full width at half maximum of peak LSPR value; $N_h$ is the density of free carriers. The density of free carriers was calculated as $7.97 \times 10^{21}$ $cm^{-3}$ according to Formula (1). When the density of free carriers was $10^{21}$ $cm^{-3}$, the characteristic absorption peak of local surface plasmons was in the NIR to MIR region [30], which was consistent with the measurement results in Fig. 7.

### 3.5. PL analysis

The emission spectra of $GdF_3$:Yb/Er and $Fe_3O_4$@$WO_{3-x(x = 0\sim1)}$@$GdF_3$:Yb/Er nanoparticles under the 980 nm excitation are as shown in Fig. 8, from which three emission peaks of $GdF_3$:Yb/Er were observed within the wavelength range of 500–800 nm. The strongest peak generated by red light emission appeared at 660 nm, which derived from $^4F_{9/2} \rightarrow {}^4I_{15/2}$ transition emission of $Er^{3+}$ ions [30]. The emission peak at 523 nm was formed by green light emission and came from $^2H_{11/2} \rightarrow {}^4I_{15/2}$ and $^4S_{3/2} \rightarrow {}^4I_{15/2}$ transition emission of $Er^{3+}$ ions [30]. The weak emission peak at 790–850 nm was generated by red light emission and ascribed to the energy level transition of $^4I_{9/2} \rightarrow {}^4I_{15/2}$ of

$Er^{3+}$ ions [31].

Compared with the emission intensity of $GdF_3$:Yb/Er nanoparticles, the emission intensity of $Fe_3O_4$@$WO_{3-x(x = 0\sim1)}$@$GdF_3$:Yb/Er nanoparticles at 523 and 660 nm evidently weakened mainly for the following reasons: (1) After the $WO_{3-x(x = 0\sim1)}$ nanoparticle layer was introduced, its LSPR effect enhanced the local electric field around $GdF_3$:Yb/Er, thus improving the emission of its up-conversion process. But the up-conversion emission may also was quenched, to a certain extent, by the direction contact between $WO_{3-x(x = 0\sim1)}$ and $GdF_3$:Yb/Er [32]; (2) The up-conversion emission of $GdF_3$:Yb/Er might be absorbed by adjacent $WO_{3-x(x = 0\sim1)}$, thus reducing the luminescent intensity [32].

It is worth noting that new emission bands of $Fe_3O_4$@$WO_{3-x(x = 0\sim1)}$@$GdF_3$:Yb/Er nanoparticles appeared within 675–775 nm, which were attributed to the energy level transition of $^4F_{9/2} \rightarrow {}^4I_{9/2}$ of $Er^{3+}$ ions. Meanwhile, the emission peak intensity of $Fe_3O_4$@$WO_{3-x(x = 0\sim1)}$@$GdF_3$:Yb/Er nanoparticles at 775–875 nm was obviously strengthened, which was attributed to the re-excitation of LSPR effect of $WO_{3-x(x = 0\sim1)}$ in the visible light region after the partial up-conversion emission of $GdF_3$:Yb/Er was absorbed by adjacent $WO_{3-x(x = 0\sim1)}$.

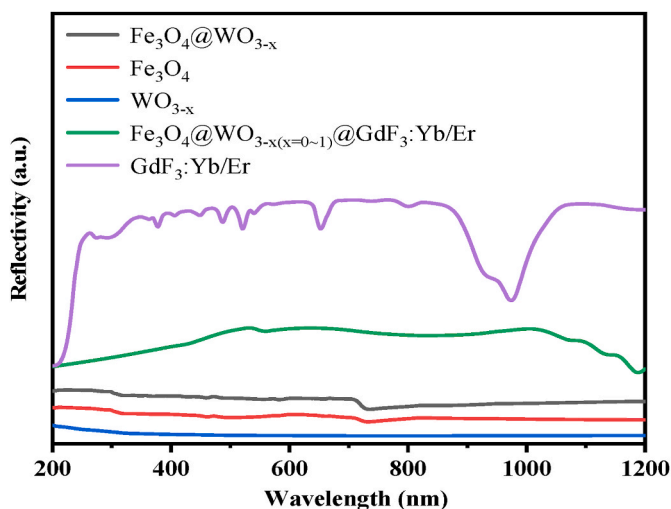**Fig. 7.** UV–Vis–NIR absorption spectra of $Fe_3O_4$, $WO_{3-x(x = 0~1)}$, $Fe_3O_4@WO_{3-x(x = 0~1)}$, $GdF_3$:Yb/Er and $Fe_3O_4@WO_{3-x(x = 0~1)}@GdF_3$:Yb/Er nanoparticles.
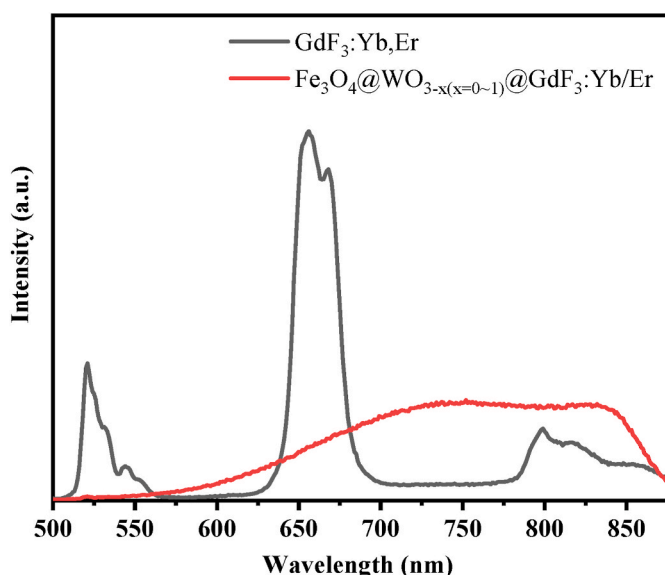


**Fig. 8.** Emission spectra of (a) $GdF_3$: Yb/Er, (b) $Fe_3O_4@WO_{3-x(x = 0~1)}@GdF_3$: Yb/Er nanoparticles.

Moreover, the number of excited $Er^{3+}$ and $Yb^{3+}$ ions was increased with the enhancement of local electromagnetic fields, so the luminescent intensity of $Fe_3O_4@WO_{3-x(x = 0~1)}@GdF_3$:Yb/Er nanoparticles in the NIR region was selectivity enhanced [33]. To sum up, the luminescence of $Fe_3O_4@WO_{3-x(x = 0~1)}@GdF_3$:Yb/Er nanoparticles was influenced, to some extent, by the LSPR effect of $WO_{3-x(x = 0~1)}$, which, moreover, could selectively enhance or weaken the luminescent of different colors.

### 3.6. Magnetic analysis

The hysteresis loop diagram of $Fe_3O_4$, $Fe_3O_4@WO_{3-x(x = 0~1)}$ and $Fe_3O_4@WO_{3-x(x = 0~1)}@GdF_3$:Yb/Er nanoparticles is displayed in Fig. 9. The three samples were observed to show similar magnetic properties. The magnetic saturation intensity of $Fe_3O_4$, $Fe_3O_4@WO_{3-x(x = 0~1)}$ and $Fe_3O_4@WO_{3-x(x = 0~1)}@GdF_3$:Yb/Er nanoparticles was 69.24 $emu \bullet g^{-1}$、4.45 $emu \bullet g^{-1}$ and 1.40 $emu \bullet g^{-1}$, respectively. In comparison with $Fe_3O_4$, the magnetic saturation intensity of $Fe_3O_4@WO_{3-x(x = 0~1)}$ and $Fe_3O_4@WO_{3-x(x = 0~1)}@GdF_3$:Yb/Er nanoparticles was

apparently reduced. The mass fraction of magnetic $Fe_3O_4$ was reduced after nonmagnetic $WO_{3-x(x = 0~1)}$ and $GdF_3$:Yb/Er nanocrystals were cladded on the surface of $Fe_3O_4$ nanoparticles. In addition, the magnetism would be degraded considerably with the increasing number of introduced nonmagnetic materials, indicating that the $WO_{3-x(x = 0~1)}$ interlayer and $GdF_3$:Yb/Er luminescent shell were successfully cladded on the surface of $Fe_3O_4$. Compared with $Fe_3O_4$, the magnetic saturation intensity of $Fe_3O_4@WO_{3-x(x = 0~1)}@GdF_3$:Yb/Er nanoparticles was reduced, but the magnetic saturation intensity of $Fe_3O_4@WO_{3-x(x = 0~1)}@GdF_3$:Yb/Er nanoparticles was enough as to deliver drugs and be applied to various fields like magnetic separation [23].

Within the same time, the magnetic responsivity of samples was observed using a magnet. The magnetic responsivity of $Fe_3O_4$, $Fe_3O_4@WO_{3-x(x = 0~1)}$ and $Fe_3O_4@WO_{3-x(x = 0~1)}@GdF_3$:Yb/Er nanoparticles after being attracted by the same magnet for 3 s is denoted by a, b and c in the illustrations of Fig. 9. It could be seen that the solution of $Fe_3O_4$ was clarified the fastest, indicating the strongest magnetism of $Fe_3O_4$ with the best magnetic response. Compared with $Fe_3O_4$ and $Fe_3O_4@WO_{3-x(x = 0~1)}$, $Fe_3O_4@WO_{3-x(x = 0~1)}@GdF_3$:Yb/Er nanoparticles were clarified the slowest, and the solution was slightly turbid, manifesting that $Fe_3O_4@WO_{3-x(x = 0~1)}@GdF_3$:Yb/Er had weaker magnetism than $Fe_3O_4$ and $Fe_3O_4@WO_{3-x(x = 0~1)}$, but it was still magnetic to some extent.

### 3.7. Microwave thermal response performance analysis

To test the microwave thermal response performance of $Fe_3O_4@WO_{3-x(x = 0~1)}@$

$GdF_3$:Yb/Er nanoparticles, the synthesized $Fe_3O_4@WO_{3-x(x = 0~1)}@GdF_3$:Yb/Er nanoparticles and the normal saline solution were respectively subjected to the microwave thermal conversion performance test. Moreover, the temperature-dependent changes in microwave radiation time within the medical microwave frequency band of 2.45 GHz were measured [13]. As shown in Fig. 10, $Fe_3O_4@WO_{3-x(x = 0~1)}@GdF_3$:Yb/Er nanoparticles were weighed and dispersed in normal saline, which served as blank control to directly explain the microwave thermal conversion performance of $Fe_3O_4@WO_{3-x(x = 0~1)}@GdF_3$: Yb/Er. The test results showed that $Fe_3O_4@WO_{3-x(x = 0~1)}@GdF_3$:Yb/Er nanoparticles were of excellent microwave thermal conversion performance. Under the sustained microwave radiation, the temperature of the nanoparticle dispersion liquid grew from 30 °C to 91 °C within 80 s, while that of normal saline rose to 33 °C under the same conditions. Compared with normal saline, the $Fe_3O_4@WO_{3-x(x = 0~1)}@GdF_3$:Yb/Er nanoparticle dispersion liquid showed the better microwave thermal conversion performance, since the $Fe_3O_4@WO_{3-x(x = 0~1)}@GdF_3$:Yb/Er nanoparticle dispersion liquid showed nanoparticle structure contained $Fe_3O_4$ and $WO_{3-x(x = 0~1)}$ with good microwave absorptivity and microwave thermal conversion performance [29]. The study results reflected the good microwave thermal conversion performance of $Fe_3O_4@WO_{3-x(x = 0~1)}@GdF_3$:Yb/Er nanoparticles, which, therefore, were suitable as the carriers to control the drug release by means of local microwave heating.

### 3.8. Drug loading and release

In this study, the chemotherapeutics—doxorubicin hydrochloride (DOX) was selected as the model drug to explore the drug loading and release capacities of $Fe_3O_4@WO_{3-x(x = 0~1)}@GdF_3$:Yb/Er nanoparticles. To avoid the influences of other factors on the experimental results, the drug loading and release experiment was performed in normal saline (9 g $L^{-1}$, simulated human body fluid) at 37 °C. The rough and loose surface of $Fe_3O_4@WO_{3-x(x = 0~1)}@GdF_3$:Yb/Er nanoparticles possessed the drug molecule loading capacity, and the DOX molecules could be connected to nanoparticles via physical absorption or hydrogen bonds so as to be loaded on the surface of $Fe_3O_4@WO_{3-x(x = 0~1)}@GdF_3$:Yb/Er nanoparticles. Then, the action force or the rupture failure of hydrogen
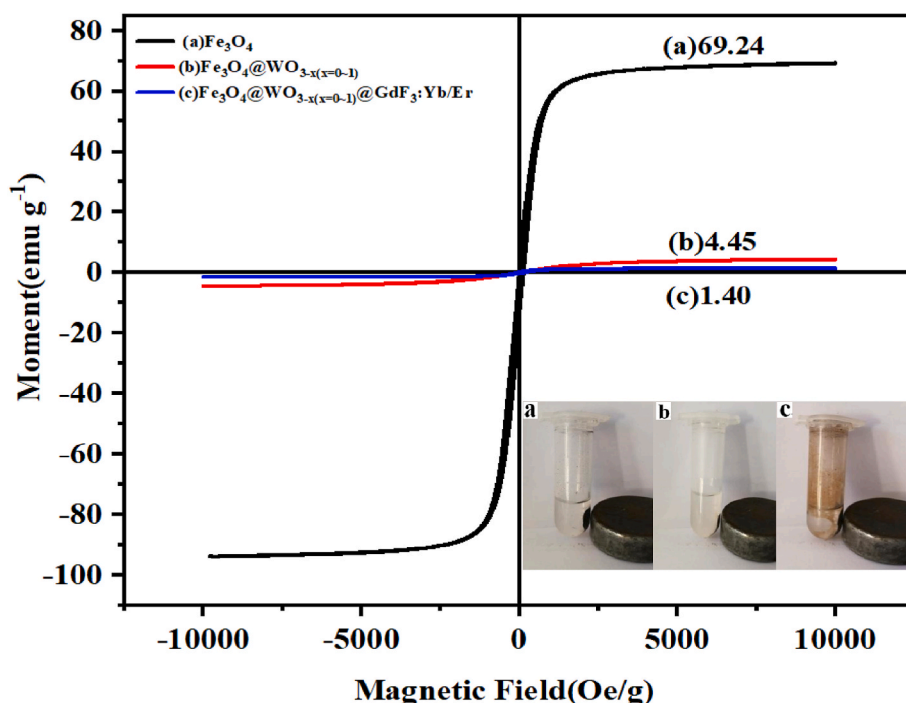
**Fig. 9.** Hysteresis loop and magnetic response of nanoparticles: (a) $Fe_3O_4$, (b) $Fe_3O_4@WO_{3-x(x\,=\,0\sim1)}$ and (c) $Fe_3O_4@WO_{3-x(x\,=\,0\sim1)}@GdF_3$:Yb/Er nanoparticles.
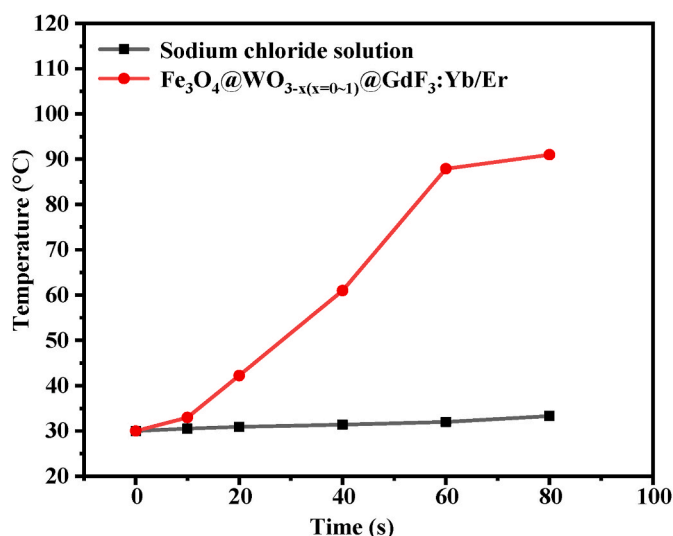


**Fig. 10.** Temperature changes of $Fe_3O_4@WO_{3-x(x\,=\,0\sim1)}@GdF_3$:Yb/Er under microwave irradiation.

bonds between the $Fe_3O_4@WO_{3-x(x\,=\,0\sim1)}@GdF_3$:Yb/Er and DOX was promoted through pH, temperature and microwave stimulation so that the drug molecules were released from $Fe_3O_4@WO_{3-x(x\,=\,0\sim1)}@GdF_3$: Yb/Er, thereby reaching the goal of microwave-controlled release.

The relationships of the drug loading process and loading rate of $Fe_3O_4@WO_{3-x(x\,=\,0\sim1)}@GdF_3$:Yb/Er nanoparticles with time at the room temperature are displayed in Fig. 11. As observed from Fig. 11 (a) and (b), the drug loading rate grew rapidly at the beginning and reached about 92.6% within 5 min, but afterwards, it grew slowly. It could be seen from the figure that DOX had the maximum absorption peak at 225 nm, and the corresponding light absorption intensity was reduced with time, indicating that the drug concentration in the solution declined with the loading time. After 150 min, about 98% of DOX molecules were loaded in the holes or the surface of $Fe_3O_4@WO_{3-x(x\,=\,0\sim1)}@GdF_3$:Yb/Er

nanoparticles, which was ascribed to their rough and loose surface and powerful absorptivity.

Fig. 12 presents the release rate-time relation graph during the drug release process of $Fe_3O_4@WO_{3-x(x\,=\,0\sim1)}@GdF_3$:Yb/Er nanoparticles at different temperatures and pH values. It could be known that at the room temperature and 37 °C, the drug release effect was not obvious, indicating that the $Fe_3O_4@WO_{3-x(x\,=\,0\sim1)}@GdF_3$:Yb/Er carrier was of good stability at the room temperature and in the normal in vivo blood circulation. At 42 °C, however, the drug release amount grew significantly with time, reaching 59.6% within 90 min, manifesting that the energy provided by the medium was higher than that needed by the acting force between nanoparticles and drug molecules. Therefore, the drug release effect was better at a high temperature.

To study the drug release conditions of $Fe_3O_4@WO_{3-x(x\,=\,0\sim1)}@GdF_3$:Yb/Er nanoparticles under different pH values, the drug release of nanoparticles was experimented in the normal saline under different pH values (temperature kept at 37 °C), as shown in Fig. 12 (b). It could be observed that 37 °C and pH = 7, only 5% of drug molecules on $Fe_3O_4@WO_{3-x(x\,=\,0\sim1)}@GdF_3$:Yb/Er nanoparticles were released within 90 min, indicating the stable acting force between $Fe_3O_4@WO_{3-x(x\,=\,0\sim1)}@GdF_3$:

Yb/Er nanoparticles and drug molecules under such conditions, which was not beneficial to the drug release. When the pH value declined to 6 and 5, the release amount of drug molecules reached 51.9% and 53.8%, respectively, since the acting force between drug molecules and nanoparticles was destructed due to the protonation effect of groups on the surface of $Fe_3O_4@WO_{3-x(x\,=\,0\sim1)}@GdF_3$:Yb/Er nanoparticles, and a large quantity of drug molecules were divorced from nanoparticles and released out. It could be known that the drug release effect was better under acidic conditions, meaning that $Fe_3O_4@WO_{3-x(x\,=\,0\sim1)}@GdF_3$:Yb/Er nanoparticles were of temperature and pH-sensitive drug release properties.

The microwave-controlled release process of the $Fe_3O_4@WO_{3-x(x\,=\,0\sim1)}@GdF_3$: Yb/Er-DOX carrier could be monitored via UV–Vis spectra. To explore the controllability, the drug release was firstly stimulated using microwave radiation, which was then stopped while the drug release was facilitated only by stirring, thus completing one cycle. The results in Fig. 13 showed that DOX drug molecules were released out in
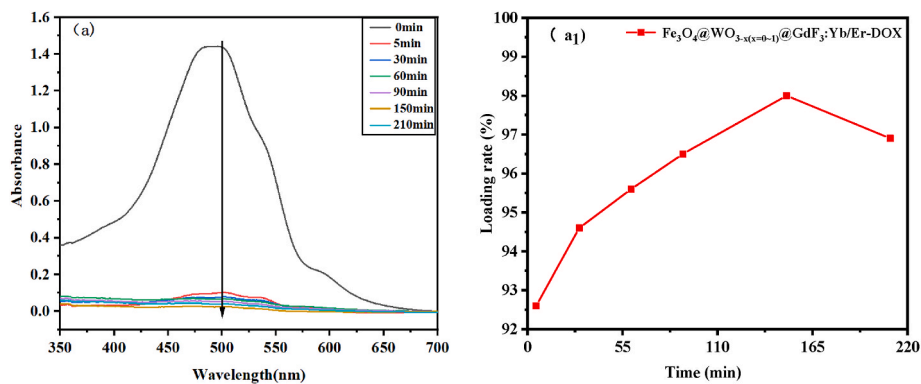
**Fig. 11.** Kinetic analysis of drug loading of $Fe_3O_4@WO_{3-x\ (x\ =\ 0\sim1)}@GdF_3$: Yb/Er nanoparticles: UV absorption spectroscopy spectrogram and drug loading rate versus time.



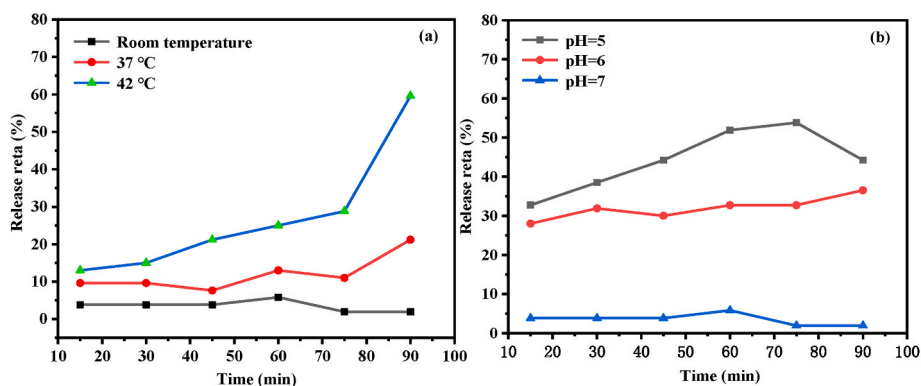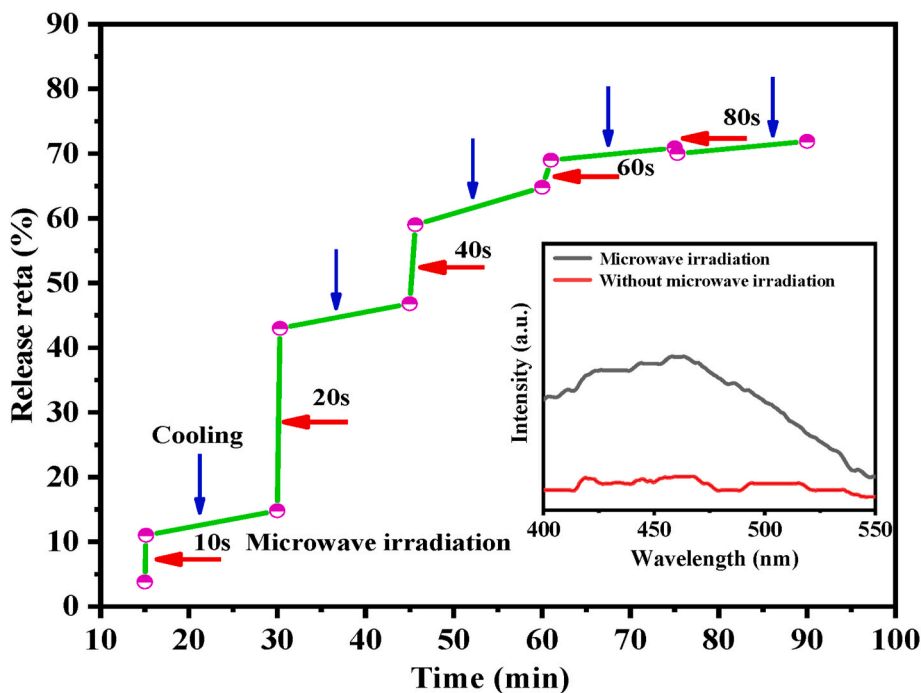**Fig. 12.** Kinetic analysis of drug release of $Fe_3O_4@WO_{3-x\ (x\ =\ 0\sim1)}@GdF_3$: Yb/Er nanoparticles.



**Fig. 13.** Controlled release profile of $Fe_3O_4@WO_{3-x(x\ =\ 0\sim1)}@GdF_3$:Yb/Er-DOX under microwave irradiation for different on/off cycles.

case of microwave radiation. The release of DOX drug molecules was repressed after the microwave generator was turned off, indicating that the microwave heating destructed the acting force between

nanoparticles and drugs and the drug molecules were released from the nanocarrier. In the initial experimental phase, about 12% of drug molecules were released out after the carrier solution was initially radiated

for 10 s. When the microwave radiation was stopped and only stirring (60 min) was done, however, only about 2% of drug molecules were released out, being much lower than the drug release rate in the event of microwave radiation. This result revealed that drug molecules could not be released when the medium temperature was lower than the critical release temperature. That's to say, the nanoparticles loaded with drugs could control the drug release accurately by regulating the on/off state of microwave radiation. As the drug release time of the carrier was lengthened, the drug release curve tended to be flat, and the release rate of drug molecules was about 70% after five cycles. Moreover, the cumulative release rate of drug molecules was elevated with the microwave radiation time, manifesting that the controlled drug release could be realized through microwave radiation, and the microwave-controlled release effect with $WO_{3-x(x\ =\ 0\sim1)}$ as the microwave absorption layer was superior to that with $ZnO$, $SnO_2$ and $TiO_2$ as the microwave absorption layer. Hence, it is feasible to use the prepared $Fe_3O_4@WO_{3-x(x\ =\ 0\sim1)}@GdF_3$:Yb/Er nanoparticles to realize the controlled drug release by regulating microwave radiation.

## 4. Conclusion

In this study, a new-type core-shell nanocarrier with magnetic, NIR luminescent and microwave heating characteristics was successfully prepared through solvothermal method and precipitation method. Its structure, morphology, performance, drug loading capacity and drug release properties were explored. The results showed that well-crystallized $WO_{3-x(x\ =\ 0\sim1)}$ and $GdF_3$:$Yb^{3+}$,$Er^{3+}$ were cladded on the surface of $Fe_3O_4$ layer by layer, thus preparing core-shell nanoparticles whose rough and loose surface could realize the effective drug loading. Under 980 nm excitation, $Fe_3O_4@WO_{3-x(x\ =\ 0\sim1)}@GdF_3$:Yb/Er nanoparticles have stronger NIR luminescence. Meanwhile, $Fe_3O_4@WO_{3-x(x\ =\ 0\sim1)}@GdF_3$:Yb/Er nanoparticles presented favorable magnetic saturation intensity and microwave heating characteristics, which facilitated targeted controlled drug delivery. Moreover, the $Fe_3O_4@WO_{3-x(x\ =\ 0\sim1)}@GdF_3$:Yb/Er nanoparticles could promote drug release through temperature, pH and microwave stimulation. Therefore, such multi-functional nanoparticles can be potentially applied to such fields as drug delivery, controllable release and microwave thermotherapy. This study will solve the bottlenecks faced in the efficient chemotherapeutics delivery of targeted drug carriers and lay a theoretical and experimental basis for the visualized real-time monitoring of chemotherapy.

## Author contribution

Ziyang Jiang and Hongxia Peng conceived and designed the experiments, and Hongxia Peng supervised the research; Wenhui Chen helped to synthesize the $Fe_3O_4@WO_{3-x(x\ =\ 0\sim1)}@GdF_3$:Yb/Er nanocomposites; Jianzhen Wu helped to examine the $Fe_3O_4@WO_{3-x(x\ =\ 0\sim1)}@GdF_3$:Yb/Er + nanocomposites; Ziyang Jiang performed the synthesis and characterization, interpreted the data and wrote the paper with help from Fabiao Yu.

## Declaration of competing interest

The authors declared that they have no conflicts of interest to this work. We declare that we do not have any commercial or associative interest that represents a conflict of interest in connection with the work submitted.

## Data availability

No data was used for the research described in the article.

## Acknowledgements

## References

[1] C. Xu, W. Liu, Y. Hu, et al., Bioinspired tumor-homing nanoplatform for co-delivery of paclitaxel and siRNA-E7 to HPV-related cervical malignancies for synergistic therapy, Theranostics 10 (7) (2020) 3325–3339.

[2] P.Y. Siboro, V.K.T. Nguyen, Y.B. Miao, et al., Ultrasound-activated, tumor-specific in situ synthesis of a chemotherapeutic agent using ZIF-8 nanoreactors for precision cancer therapy, ACS Nano (2022), https://doi.org/10.1021/acsnano.2c03587.

[3] L. Sha, Y.J. Wu, F. Ding, et al., Engineering macrophagederived exosomes for targeted chemotherapy of triple negative breast cancer, Nanoscale 12 (2020) 10854–10862.

[4] C.L. Wang, X.J. Wang, W. Zhang, et al., Shielding ferritin with a biomineralized shell enables efficient modulation of tumor microenvironment and targeted delivery of diverse therapeutic agents, Adv. Mater. 34 (5) (2022) 2107160–2107160.

[5] Y. Ju, H.T. Liao, J.J. Richardson, et al., Nanostructured particles assembled from natural building blocks for advanced therapies, Chem. Soc. Rev. 51 (2022) 4287–4336.

[6] X.S. Li, J.H. Kim, J.Y. Yoon, et al., Cancer-associated, stimuli-driven, turn on theranostics for multimodality imaging and therapy, Adv. Mater. 1606 (2017) 857–881.

[7] L. Rao, L.L. Bu, Q.F. Meng, et al., Antitumor platelet-mimicking magnetic nanoparticles, Adv. Funct. Mater. 279 (2017) 1604774–1604784.

[8] D.O. Zhuang, H.F. Zhang, G.W. Hu, et al., Recent development of contrast agents for magnetic resonance and multimodal imaging of glioblastoma, J. Nanobiotechnol. 201 (2022) 1479–1486.

[9] S.G. Gai, P.P. Yang, C.X. Li, et al., Synthesis of magnetic, up-conversion luminescent,and mesoporous core–shell-structured nanocomposites as drug carriers, Adv. Funct. Mater. 20 (2010) 1166–1172.

[10] L. Cheng, C. Wang, X. Ma, et al., Multifunctional upconversion nanoparticles for dual-modal imaging-guided stem cell therapy under remote magnetic control, Adv. Funct. Mater. 23 (3) (2013) 272–280.

[11] X. Cui, D. Mathe, N. Kovács, et al., Synthesis, characterization and application of core-shell Co0.16Fe2.84O4@NaYF4 (Yb, Er) and Fe3O4@NaYF4 (Yb, Tm) nanoparticle as tri-modal (MRI, PET/SPECT and Optical) imaging agents, Bioconjugate Chem. 27 (2) (2016) 319–328.

[12] R.L. Wang, M. He, Y.M. Zhou, et al., Metal−organic frameworks self-templated cubic hollow Co/N/C@MnO2 composites for electromagnetic wave absorption, Carbon 156 (2019) 378–388.

[13] Y. Zhao, Z. Zhou, G.X. Chen, et al., Coaxial double-layer-coated multiwalled carbon nanotubes toward microwave absorption, Mater. Lett. 233 (2018) 203–206.

[14] H. Feng, J. Huang, X. Wang, et al., Microstructure and enhanced electromagnetic wave absorbing performance of Zn0.6Ni0.3Cu0.1Fe2O4 ferrite glass-ceramic, Ceramic international (7) (2022) 48–56.

[15] X. Sun, Micro-structural design of CoFe2O4/SWCNTs composites for enhanced electromagnetic properties, Coatings (2022) 12–21.

[16] K. Zhao, F. Ye, L. Cheng, et al., Synthesis of embedded ZrC-SiC-C microspheres via carbothermal reduction for thermal stability and electromagnetic wave absorption, Appl. Surf. Sci. (2022) 591–598.

[17] Z. Xiang, Y.M. Song, J. Xiong, Enhanced electromagnetic wave absorption of nanoporous Fe3O4@carbon composites derived from metal-organic frameworks, Carbon 142 (2019) 20–31.

[18] L. Liu, D. Han, L. Shi, et al., Fabrication and microwave absorbing property of WO3@WC with a core-shell porous structure, Ceramic international (18) (2022) 48–59.

[19] H. Wang, H. Ma, Enhancing the microwave absorbing properties of molybdenum dioxide by designing a double-layered structure, Mater. Res. Bull. 122 (2020) 110692.1–110692.5.

[20] H. Li, J. Wang, Y. Huang, et al., Microwave absorption properties of carbon nanotubes and tetrapod-shaped ZnO nanostructures composites, Mater. Sci. Eng. B 175 (1) (2010) 81–85.

[21] S. Shi, S. Hao, C. Yang, et al., Enhanced microwave absorption properties of reduced graphene oxide/TiO2 nanowire composites synthesized via simultaneous carbonation and hydrogenation, J. Mater. Chem. C (25) (2022) 10–18.

[22] Z. Deng, S. He, W. Wang, et al., Construction of hierarchical SnO2@Fe3O4 nanostructures for efficient microwave absorption, J. Magn. Magn Mater. (2019) 498–506.

[23] H.X. Peng, Y. He, X.Y. Tian, et al., LSPR effects in a magnetic–luminescent heterostructure for efficient enhanced luminescence performance, New J. Chem. 43 (2019) 304–311.

[24] R. Yan, Y.J. Guo, X.C. Wang, et al., Near-infrared light-controlled and real-time detection of osteogenic differentiation in mesenchymal stem cells by upconversion nanoparticles for osteoporosis therapy, ACS Nano 16 (2022) 8399–8418.

[25] Y. Yang, J.S. Huang, W. Wei, Switching the NIR upconversion of nanoparticles for the orthogonal activation of photoacoustic imaging and phototherapy, Nat. Commun. 13 (2022) 31–49.

[26] O. Balitskii, D. Moszynski, Z. Abbas, Aqueous processable WO3-x nanocrystals with solution tunable localized surface plasmon resonance, RSC Adv. 6 (2016) 59050–59054.

[27] Q. Huang, S. Hu, J. Zhuang, $MoO_{(3-x)}$-based hybrids with tunable localized surface plasmon resonances: chemical oxidation driving transformation from ultrathin nanosheets to nanotubes, Chemistry 18 (48) (2012) 15283–15286.

[28] Z. Zhang, L. Yang, Y.R. Fang, Near-infrared-plasmonic energy upconversion in a nonmetallic heterostructure for efficient $H_2$ evolution from ammonia borane, Adv. Sci. 180 (2018) 748–758.

[29] H.X. Peng, J.D. Ouyang, Y.X. Peng, A simple approach for the synthesis of bi-functional $Fe_3O_4@WO_{3-x}$ core–shell nanoparticles with magnetic-microwave to heat responsive properties, Inorg. Chem. Commun. 84 (2017) 138–143.

[30] W.J. Zeng, H.X. Peng, J.Z. Wu, Up-down conversion luminescence and drug-loading capability of novel $MoO_{3-x}$ based carriers, Adv. Powder Technol. 32 (2021) 4373–4383.

[31] P. Anna, O.B. Joanna, Plasmonic enhancement of two-photon excited luminescence of gold nanoclusters, Molecules (2022), https://doi.org/10.3390/molecules27030807.

[32] K. Chen, L.L. Gong, S.J. Ding, Tunable charge transfer and dual plasmon resonances of $Au@WO_{3-x}$ hybrids and applications in photocatalytic hydrogen generation, Plasmonics 15 (2020) 21–29.

[33] Q.C. Sun, M. Haridas, J.C. Ribot, Plasmon-enhanced energy transfer for improved upconversion of infrared radiation in doped-lanthanide nanocrystals, Nano Lett. 141 (2014) 101–106.